Solar wind density influence on geomagnetic storm intensity

R. S. Weigel[1]

[1]   Solar wind density has been argued to have a strong effect on geomagnetic storms. Elevated solar wind density tends to occur in time intervals when the solar wind electric field is large. This complicates the analysis required to identify a solar wind density influence because the solar wind electric field is the dominant driver of geomagnetic storms. Statistical studies have consistently shown that the independent correlation between solar wind density and geomagnetic storm intensity (via a proxy, such as the D_{st} index) is small. Modeling considerations predict a significant geomagnetic storm dependence on the plasma sheet density, which is indirectly connected to solar wind density. In this work, the solar wind density influence is quantified using two statistical measures: (1) data-derived impulse response functions and (2) the relationship between the integrated value of D_{st} to the integrated value of the solar wind electric field during geomagnetic storm intervals. Results from both approaches indicate that the solar wind density modifies the geoefficiency or the ability of a given value of the solar wind electric field to create a D_{st} disturbance. The impulse response method also predicts that solar wind density explains the difference in geoefficiency, as opposed to the solar wind dynamic pressure. Although the geoefficiency effect is large, its influence is shown to be small when only large storms are considered because large storms typically have large density.

1.   Introduction

[2]   The role of the solar wind density, N_{sw}, on solar wind magnetosphere coupling is not straightforward. Statistical studies generally find that the best predictor of geomagnetic indices such as D_{st} does not depend strongly on an input (or "driver") function that contains N_{sw} [*Wu and Lundstedt*, 1997; *O'Brien and McPherron*, 2000]. However, others have argued that N_{sw} should play a role in mediating the energy transferred to the inner magnetosphere from the solar wind. *Borovsky et al.* [1998] showed a correlation between N_{sw} and the plasma density at geosynchronous orbit in Earth's magnetosphere and suggested a connection by a mechanism that involved the transport of solar wind plasma via the plasma sheet boundary layer, convection in the near-Earth plasma sheet, and eddy diffusion. Inner magnetosphere simulations predict that the density of ions and electrons near geosynchronous orbit should influence ring current amplitude [*Liemohn et al.*, 2001; *Jordanova et al.*, 2003].

[3]   *Borovsky and Denton* [2006] studied the differences between storms generated by corotating interaction regions (CIRs) and coronal mass ejections (CMEs) and found that the CME-driven storms have a denser plasma sheet and are larger on average and proposed that plasma sheet preconditioning may play a role in explaining the fact that CME-driven storms are larger on average. *Borovsky and Denton* [2006] also noted that CME-driven storms have larger magnetospheric convection, which is primarily driven by the solar wind electric field. *Lavraud et al.* [2006] showed that D_{st} for both CME- and CIR-driven geomagnetic storms with extended prior periods of northward interplanetary magnetic field (IMF) were typically underpredicted by a model and noted that this is consistent with the hypothesis that a plasma sheet preconditioned with high density will cause a larger-than-average geomagnetic storm because extended periods of northward IMF result in a high density plasma sheet [*Thomsen et al.*, 2003]. Besides the preconditioning mechanism, other N_{sw} effects on the magnetosphere have been documented or proposed.

[4]   *Lopez et al.* [2004] showed that high N_{sw} causes a change in the compression ratio of the bow shock for strong and southward IMF, which is typically associated with geomagnetic storms and an enhanced ring current. The predicted effect is an increased sensitivity to N_{sw} for large southward IMF. Global magnetohydrodynamics (MHD) simulation diagnostics of Joule heating and polar cap potential were shown to be consistent with the predictions of this mechanism.

[5]   Solar wind density can also affect magnetospheric response through the solar wind dynamic pressure $P_{dyn} = N_{sw}v^2$, where v is the solar wind velocity along the Sun-Earth line. *Xie et al.* [2008] developed a model where solar wind dynamic pressure plays a role in preconditioning the magnetosphere that was motivated by the *Siscoe et al.* [2002]

---

[1]Department of Computational and Data Sciences, George Mason University, Fairfax, Virginia, USA.
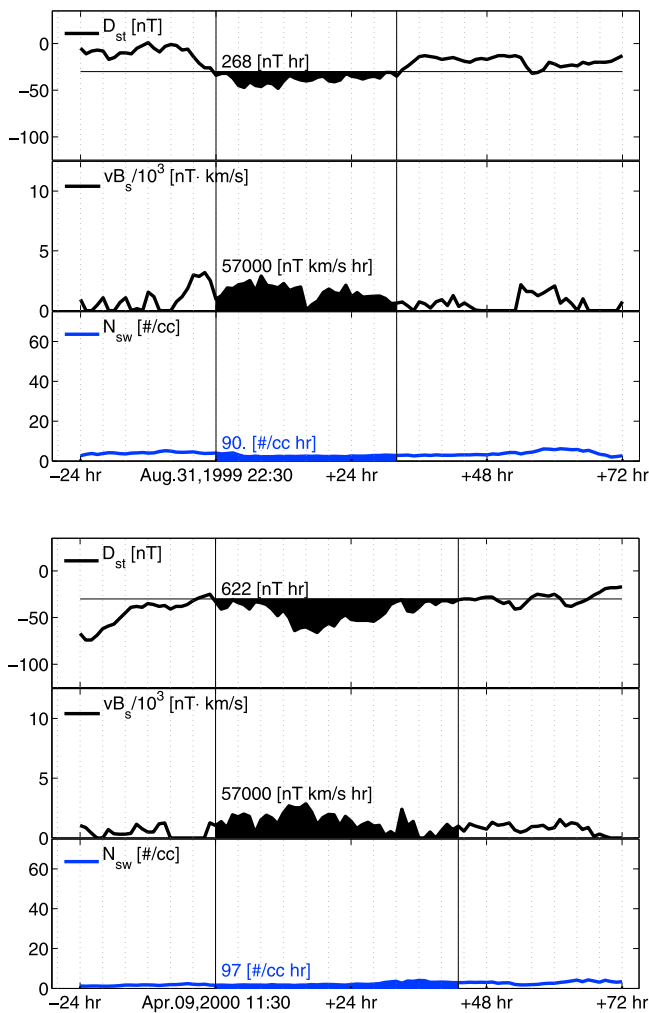
Figure 1. Time series associated with two low N_{sw} intervals that are part of the ensemble of events considered in section 2.2. The integrated areas are filled in, and the value of the integral is indicated in text.

study which found that a MHD simulation predicts a polar cap potential saturation with a $P_{dyn}^{2/3}$ dependence. *Wang et al.* [2003] found a relationship between the decay time constant parameter in a model of ring current injection and solar wind pressure for northward IMF. An event study by *Shi et al.* [2005] showed that the solar wind density had an effect on the ring current asymmetry.

[6] *Shue and Kamide* [2001] showed a close correlation between solar wind density and auroral zone ground magnetic field perturbations for an event on 10 January 1997. Because the correlation took place on a very short timescale (∼10 min), they argued that the response was not explained by the *Borovsky et al.* [1998] mechanism that acts on the order of 2–6 h. The statistical study by *Shue et al.* [2005] found that for intervals where all other solar wind variables are nearly constant, the auroral electroject indices increase or decrease with equal probability given an impulse in N_{sw}.

[7] *Boudouridis et al.* [2005] considered ionospheric flow and particle data for three events and found that a sudden increase in solar wind dynamic pressure led to an increase in coupling efficiency, where the coupling efficiency was

defined as the ratio of the cross-polar-cap potential to the cross-magnetospheric potential in the undisturbed solar wind.

[8] There are many possible mechanisms by which the solar wind density can affect the magnetosphere. In this work we attempt to reconcile the observation that solar wind density statistically has a small signature in correlation-type studies while other results find evidence or predict a large N_{sw} effect on D_{st}. We also quantify the N_{sw} effect and compare our results with those from the works described above.

2. Analysis

[9] The statistical analyses performed here are all based on the separation of data according to the amplitude of N_{sw}. In section 2.1, all data are used while in section 2.2, only data in time intervals where D_{st} was disturbed are used.

[10] The term "geoeffective" is usually used in reference to the near-Earth IMF orientation during the passage of a large-scale solar wind structure such as a CME or CIR. Here we use the term "geoefficiency" in the same sense as mechanical efficiency, that is, the amount of output (in terms of magnetospheric response) to a fixed unit of input.

[11] Two measures of geoefficiency are considered. In section 2.1 it is the predicted amplitude of the response of D_{st} to an impulse in the solar wind electric field, $E_{sw} = vB_s$. In section 2.2 it is the ratio of the time-integrated value of D_{st} to the time-integrated value of vB_s during active D_{st} intervals.

[12] Before presenting the results of the statistical analysis, we present a few intervals of data that make up the ensemble of events used in this study. Example intervals of low and high N_{sw} are shown in Figure 1 and Figure 2, respectively. All four of these intervals had approximately the same integrated input of $\int vB_s \, dt \sim 0.56 \cdot 10^5$ (km/s·nT·h) (56 mV/m·h) over the time that D_{st} was active (taken to be when it was less than −30 nT). The intervals shown in Figure 1 had a weak D_{st} response and a low and steady N_{sw} before the start of the activation. Both intervals shown in Figure 2 had an elevated or increasing solar wind density prior to the start of the activation interval.

[13] Comparison of the intervals shown in Figure 1 with Figure 2 may seem to indicate a clear association between low N_{sw} and a small D_{st} response. However, not all observations are consistent with this association, indicating that if there is a D_{st} dependence on N_{sw}, it is not as straightforward or obvious as the D_{st} dependence on vB_s. For example, in the event shown in Figure 2 (top), there was a spike in N_{sw} before the start of the disturbance in D_{st}. However, both events in Figure 2 had similar integrated values of D_{st}, vB_s, and N_{sw} during the activation time. Therefore if elevated N_{sw} prior to the storm influences the overall geomagnetic storm level, the storm shown in Figure 2 (top) should have been larger.

2.1. Impulse Response

[14] One approach for identifying relationships between solar wind measurements and geomagnetic parameters uses forward modeling where a base model is assumed and improvements in model performance given changes in the base model are sought. The base model used for the pressure-corrected D_{st}, D_{st}^* is typically that from [*Burton et al.*, 1975]:

$$dD_{st}^*/dt = -D_{st}^*/\tau + Q(t), \tag{1}$$
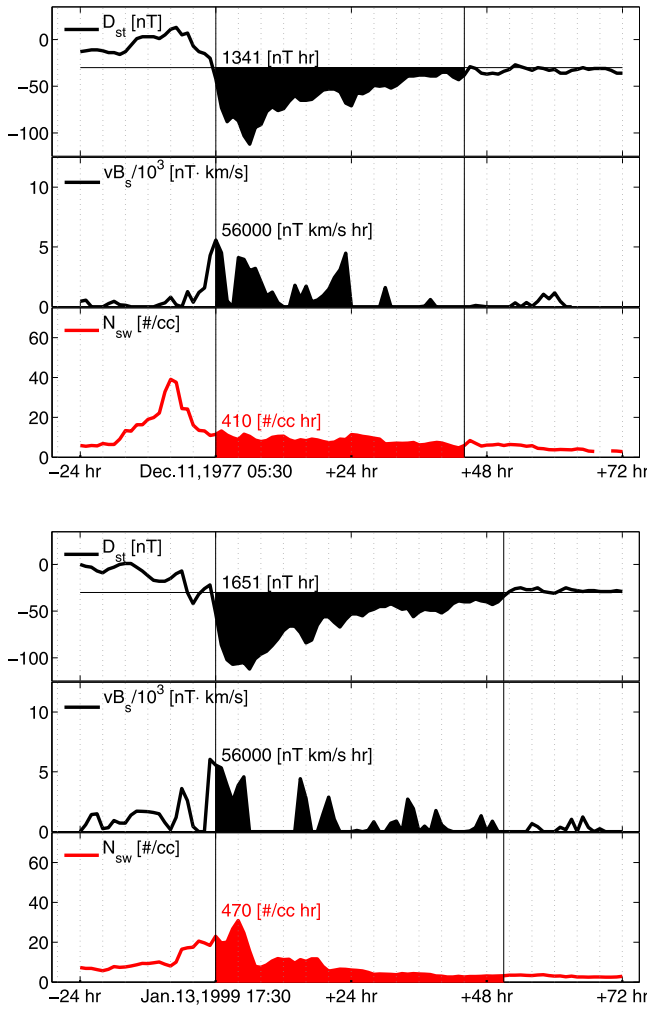
Figure 2. Time series associated with two high N_{sw} intervals that are part of the ensemble of events considered in section 2.2. The integrated areas are filled in, and the value of the integral is indicated in text. Compared to the events shown in Figure 1 the integrated vB_s values are nearly the same, within 1%, but the integrated values of N_{sw} and D_{st} are much larger.

where the star superscript is used to indicate that any contribution from the solar wind pressure-generated magnetopause current has been removed from the measured D_{st}; Q is a solar wind coupling (or driving) variable that represents the injection of energy into the ring current and is usually prescribed as being proportional to $E_{sw} = vB_s$. Given this model, ad hoc parameterizations that include a dependence on other solar wind variables can be used, for example,

$$dD_{st}^*/dt = -f(N_{sw}, v, B_s)D_{st}^* + g(N_{sw}, v, B_s)Q(t). \quad (2)$$

The procedure for hypothesis testing of different mechanisms is to introduce free parameters in f and/or g and then search for parameter values for which some measure of the prediction error is minimized. This approach was taken by *O'Brien and McPherron* [2002] who used $f = 1/\tau(vB_s)$ to parameterize a decay time, τ, dependence on the solar wind electric field vB_s. Both *Wang et al.* [2003] and *Xie et al.* [2008]

showed that using $g = g(P_{dyn})$ gives an improved data-model comparison. *Lavraud et al.* [2006] showed that a form of equation (2) tended to underestimate the actual D_{st}^* for storms that were preceded by extended periods of northward IMF (although the differences were noted to be on the order of the error bars).

[15] One difficulty with this approach is that different nonlinear modifications of the base model, motivated by different physical processes, may give equal improvements in the model's prediction error and so the conclusion on the influence of a given process is not unique without further analysis.

[16] An alternative approach to isolating mechanisms with solar wind dependencies begins with inverse modeling using a discretization of the linear continuous differential equation given by equation (1)

$$D_{st}^*(t) = h_\Delta + \sum_{t'=-N_a}^{N_c} Q_{t-t'}h_{t'}, \quad (3)$$

where $h_{t'}$ are constant coefficients that depend on τ, h_Δ is an offset constant, and N_a and N_c are integers representing the maximum time lag of the acausal and causal part of the response, respectively. In the limit that $N_a = 0$ and $N_c = 0$, equation (3) is a linear regression that relates D_{st} to the input driver function Q at time t; works that use this type of linear regression typically find that the optimal value of Q depends on either the solar wind dynamic pressure, solar wind density, or combinations thereof [*Perreault and Akasofu*, 1978; *Newell et al.*, 2007]. (As will be discussed, the relevance of coupling functions more complex than E_{sw} is questionable because as N_a and N_c are increased, the improvement of more complicated functions over $Q \sim E_{sw}$ diminishes.) Although equation (3) is linear, one can systematically isolate different nonlinear solar wind effects by computing h under different solar wind conditions. In this work we look for a $h = h(N_{sw})$ dependency by splitting the data used to compute these coefficients by the amplitude of N_{sw}.

[17] One advantage of the inverse approach is that if h_t/h_{t+1} is not constrained, equation (3) is a generalization of equation (1). Equation (3) can accommodate an additional process that has a delay τ_a in activation and a decay time of τ_2, equivalent to adding a term $Q(t - \tau_a)/\tau_2$ to equation (1). (A process with such a time delay was suggested by *Kamide et al.* [1998]). Another possible solution is that D_{st} is related to Q via a second-order linear differential equation [*Vassiliadis et al.*, 1999].

[18] It is customary to model the measured D_{st} to the pressure corrected value by $D_{st} = D_{st}^* + bP_{dyn}^{1/2} + c$, with D_{st}^* being the pressure-corrected value, $P_{dyn}^{1/2}$ a term that accounts for the magnetopause current contribution to D_{st}, and b and c being adjustable parameters. In this case the discretization can be written

$$D_{st}(t) = h_\Delta + \sum_{t'=-N_a}^{N_c} Q_{t-t'}h_{t'} + \sum_{t'=-N_a}^{N_c} P_{dyn\ t-t'}^{1/2}h_{t'}^P \quad (4)$$

and the parameters b and c are reflected in the h^P coefficients. Note that when equation (1) is discretized after rewriting it in terms of D_{st}, the pressure-correction coefficients are related, but no constraints are imposed here when solving
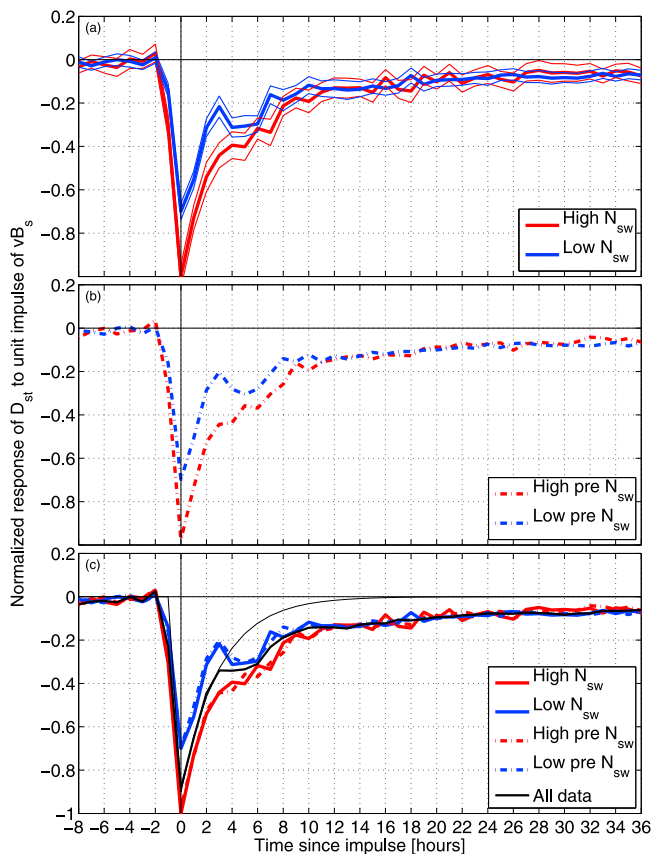
Figure 3. Impulse response functions derived using hourly averaged D_{st} and vB_s data when (a) N_{sw} was high or low in the same time interval or (b) the sum of the previous 4 hours of N_{sw} was high or low. (c) Impulse response functions from Figures 3a and 3b overlaid along with the impulse response derived using all data without separation by N_{sw}. Thin lines in Figure 3a indicate the 97% error bar levels for the impulse response amplitude. The thin black line in Figure 3c is an exponential decay curve with a time constant selected so that it matched the first 3 h of the IRF derived using all data.

equation (4). Note that our conclusions are the same when this pressure correction term is not included.

[19] The regression parameters $h_{t'}$ and $h_{t'}^P$ are computed by solving the overdetermined set of equations generated by preparing N 1-h resolution D_{st} values and the associated right-hand side of equation (4). All parameters are taken from the OMNI2 data set of *King and Papitashvili* [2005] when it included data through December 2007 (the hourly average D_{st} index in this data set is from the WDC for Geomagnetism, Kyoto). N_{sw} is the proton density measured by a satellite in the solar wind upstream of the bow shock.

[20] In this work we use only $Q = vB_s$ as we have found that when enough time delays are used, it performs at the same level or slightly better than more complex coupling functions. As an example, if $N_a = N_c = 0$ the "universal coupling function" from *Newell et al.* [2007] is approximately ~15% better than $Q = vB_s$, the same when $N_a = N_c = 6$, and slightly worse when N_a and N_c are greater than about 15.

[21] An interpretation of this result is that the true input solar wind driver is simply the solar wind electric field, but when an approximate model is used that does not account for

all of the time delays in the system, complex coupling functions produce better results because an additional variable in it is acting as a surrogate for the missing time delay component of the model. This interpretation is consistent with the result of *Weigel* [2007] who showed that when a model that includes time delays is used, the amount of the semiannual variation in geomagnetic activity that could be explained by the solar wind significantly increased.

[22] In this work we use $N_a = N_c = 48$. With this choice, the average change in the difference between the high and low response functions when the total length of the response filter was doubled to $2(N_a + N_c)$ was less than 10%. Besides finite time lags, there are other factors that may cause the computed impulse response functions to differ from the true response functions, including the fact that we are using hourly average data. However, these factors are not expected to affect our conclusions because we are looking for differences in impulse response functions, and these factors can be reasonably assumed to not depend on N_{sw}.

[23] Figure 3a shows the impulse response function computed by categorizing the set of equations of equation (4) by N_{sw} according to either whether at $t' = 0$ there was low N_{sw} (the lower 50% of the ~160,000 intervals) or high N_{sw} (the highest 50% of the intervals). The median value of N_{sw} is 5.3/cm^3. The impulse response function for both the high and low intervals was computed 50 times using a different random sample of one-half of the available equations in each category (~40,000), and the average is shown with a heavy line.

[24] When separated by N_{sw}, the impulse response coefficients h_t can be interpreted as the expected response of D_{st} to a one–hour impulse of Q under conditions of low and high N_{sw} at the time of the impulse. Figure 3a shows that the impulse response has a strong dependence on N_{sw}. Under conditions of high N_{sw}, the minimum D_{st} value is approximately 40% lower. The average value of N_{sw} was 10.5/cm^3 for the high and 3.0/cm^3 for the low category.

[25] The error bar associated with each h value was estimated using a resampling approach. This error bar is taken as the value of two times the standard deviation of 50 impulse response functions, each of which was generated by taking a random selection of one-half of the possible equations in each category.

[26] The total uncertainty is shown by the thin upper and lower lines in Figure 3a. In order to simplify the presentation, in subsequent figures we do not show these upper and lower error bounds, but they have been computed and are commented on as appropriate. These lines represent both the variation in the impulse response curves that are due to the subset of data used to compute the impulse response function and the uncertainty due to the finite length of the impulse response function mentioned above.

[27] The result of Figure 3a is consistent with the preconditioning hypothesis in that it predicts a higher N_{sw} will allow a given solar wind impulse to result in a larger response of D_{st}. An additional prediction of this hypothesis is that the effect should depend on the average N_{sw} prior to the impulse. We can test this prediction by recalculating the impulse response functions after separating the data according to the integrated N_{sw} over the hours $t' = -3, -2, -1$, and 0 instead of the instantaneous value N_{sw} at $t' = 0$ as done for Figure 3a. This result is shown in Figure 3b. The average values of N_{sw}
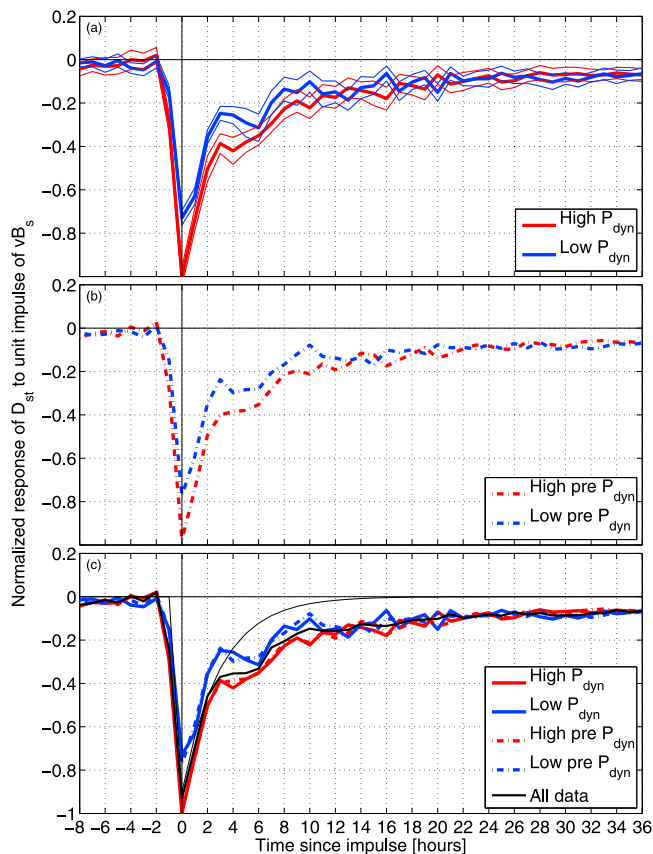
Figure 4. Impulse response functions derived by using only D_{st} and vB_s data when (a) P_{dyn} was high or low in the same time interval or (b) the sum of the previous 4 h of P_{dyn} was high or low. (c) Impulse response functions from Figures 4a and 4b overlaid along with the impulse response derived using all data without separation by N_{sw}.

were 10.4/cm^3 for the high interval and 3.4/cm^3 for the low interval.

[28] Figure 3c compares the cases shown in Figure 3a and 3b. The impulse response functions for the high and low N_{sw} subsets are not statistically different, which may not have been expected if preconditioning was the primary factor or may be an indication that a more sensitive statistical test is needed. (The result is similar if $t' = -7, \ldots, 0$ is used.) By not statistically different, we mean that the error bars (not shown) associated with, for example, one of the high N_{sw} IRF curves are such that the other high N_{sw} IRF curve falls within these error bars 90% of the time, and vice versa.

[29] Figure 3c also shows the impulse response curve derived without separation by N_{sw} as a thick black line. The thin black line is an exponential curve with a decay constant selected to match this curve from $t = 0$ through $t = 3$. An exponential impulse response is expected from equation (1). The meaning of the differences between the exponential and the data-derived impulse response functions is covered in section 4.

[30] *Xie et al.* [2008] argued that the solar wind dynamic pressure plays a role in preconditioning the magnetosphere. They modeled this by modifying equation (2) to include a P_{dyn} dependence in Q, and a vB_s and P_{dyn} dependence in τ. Figure 4a shows the impulse response function computed for

both high and low solar wind dynamic pressure, $P_{dyn} = N_{sw}v^2$. To determine if the difference between them is simply due to the fact that P_{dyn} is proportional N_{sw}, we have recalculated Figure 4 using only v^2; this result is shown in Figure 5. The impulse response functions are much less sensitive to the average value of v^2, and the ordering of the low and high curves is actually opposite of that for N_{sw} at lags of 0, 1, and 2 h. This result indicates that the differences shown in Figure 4a are due to primarily a N_{sw} and not P_{dyn} effect.

2.2. Integrated Response

[31] An alternative approach to determining the influence of N_{sw} on D_{st} response is to compare the integrated value of D_{st} when it crosses below a threshold value to the integrated value of vB_s in the same time interval. The ratio of these two integrals represents a geoefficiency or the efficiency by which a continued input in vB_s is converted into a continued disturbance in D_{st}.

[32] If geoefficiency depends on an auxiliary variable, then the average of the ratios of the integrated D_{st} to integrated vB_s in storm-like intervals should also depend on this auxiliary variable. For this analysis, we define storm-like intervals as when D_{st} was below -30 nT for at least 15 h. The integrated input is the sum of vB_s over the time interval when D_{st} was
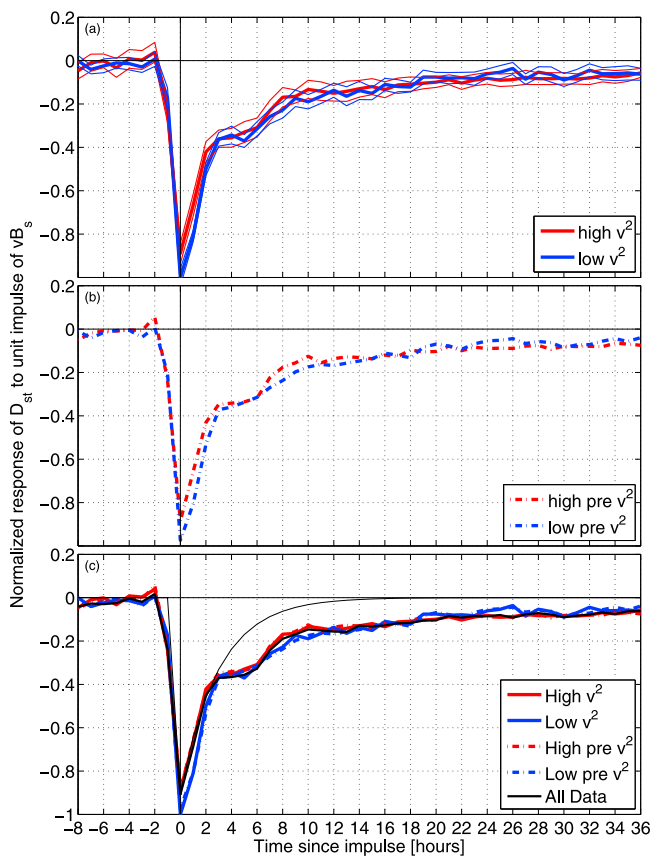
Figure 5. Impulse response functions derived by using only D_{st} and vB_s data when (a) v^2 was high or low in the same time interval or (b) the sum of the previous 4 h of v^2 was high or low. (c) Impulse response function for Figures 5a and 5b overlaid along with the impulse response derived using all data without separation by N_{sw}.
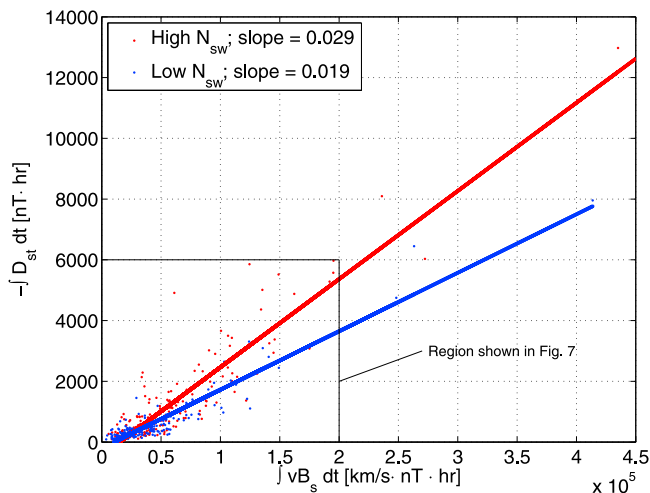
Figure 6. Sum of D_{st} and vB_s for 416 intervals for which D_{st} remained below −30 nT for at least 15 h and was preceded and followed by 2 h of $D_{st} > -30$ nT. The box outlines the region shown in Figure 7.

below −30 nT. Figures 1 and 2 discussed previously contain four example intervals that fit these criteria.

[33] Because there is a time delay in D_{st} response when vB_s becomes nonzero, and a dissipation time for D_{st} to become small after vB_s becomes zero, the integration window for vB_s should be shifted in time with respect to the integration time for D_{st}. Time shifts in vB_s from zero to 3 h were tested.

[34] Figure 6 shows 416 intervals that satisfied the storm-like criterion separated in half and color coded according to the integrated value of N_{sw} in the time interval during which $D_{st} < -30$ nT. The intervals with high N_{sw} are much more extended in vB_s and D_{st} while those for low N_{sw} are clustered near the lower left. This difference is due to the fact that the solar wind conditions for geoeffective CMEs is typically high N_{sw} with an extended duration of southward IMF [*Borovsky and Denton*, 2006]. The fact that the high N_{sw} intervals cover a much larger range in integrated D_{st} does not necessarily mean that vB_s in these intervals was more geoefficient. The important geoefficiency measure is the ratio of the integrated responses, which we have computed using a linear regression of the data points for both the low and high N_{sw} intervals. The ratio of the high to low slopes shown in Figure 6 is 1.5 ± 0.1.

[35] To determine if the slope ratio depends on the size of the storm, we have computed the slopes using only events for which the integrated value of the solar wind electric field was less than $1.0 \cdot 10^5$ (km/s·nT·h). Figure 7 shows data from Figure 6 that satisfy this condition. For these events, the slope is still larger for high N_{sw} and the high-to-low slope ratio is again 1.5 ± 0.1.

[36] The slope is not strongly dependent on the choice of thresholds, the choice of the length of time D_{st} must be below the threshold, or the amount of shift in the averaging window for vB_s and N_{sw}. Variation of these parameters yielded changes in the slope ratio on the order of $\pm 10\%$.

[37] The fact that most large storms fall into the large density category means that any study of storms will be biased toward the results for the high-density category. For example, if we do the analysis on the CME storms of

Richardson et al. [2002] (also studied by *Lavraud et al.* [2006]), a much less significant density effect is found. This is explained by the fact that 80% of the storms identified in the list fall in the high-density event category of events shown in Figure 6. This relationship is clear in the epoch averages of the high and low-density data from Figure 6 shown in Figure 8. Both $-D_{st}$ and vB_s are lower for the low N_{sw} epoch curves.

[38] The data derived impulse response functions shown in Figure 3a can be subjected to the integral analysis performed in this section. In this case the ratio of integrated D_{st} between the response functions derived using high versus low density data gives a slope ratio 1.5 ± 0.1.

3. Quantification of the Geoefficiency/Density Relationship

[39] To quantify the geoefficiency dependence on N_{sw}, we have reexecuted the experiment performed in section 2.1 except that instead of computing two impulse response functions (IRFs), one for low and one for high N_{sw}, we have computed 25 impulse response functions. Each IRF was computed using a sliding window with 20% of the available data sorted on N_{sw}. The result is shown in Figure 9a. The values for the first definition of geoefficiency, η, the magnitude of the peak of the IRF, are shown by magenta dots along with a best-fit line. In Figure 9, all η values were scaled by the best-fit line η value for the lowest N_{sw} bin.

[40] The geoefficiency based on the second definition, the ratio of the integrated output, given by the cumulative sum of the IRF, is shown with black dots. This geoefficiency measure has a larger slope which reflects the fact that the magnitude of the IRFs for high N_{sw} are higher at many points, not just at the peak. This slope indicates that given two geomagnetic storms where the density was on average 2 protons/cm^3 versus 12 protons/cm^3, but the vB_s condi-
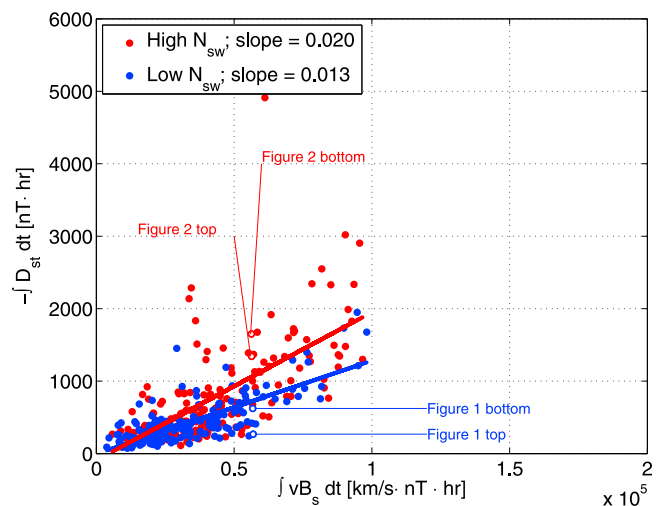
Figure 7. Zoom-in of the range indicated by the box in Figure 6. The linear regression lines were computed using only data with an integrated electric field less than $1.0 \cdot 10^5$ (km/s·nT·h). The data associated with the four dots with white centers at $\int vB_s \, dt \sim 0.56 \cdot 10^5$ (km·/snT·h) are shown in Figures 1 and 2.
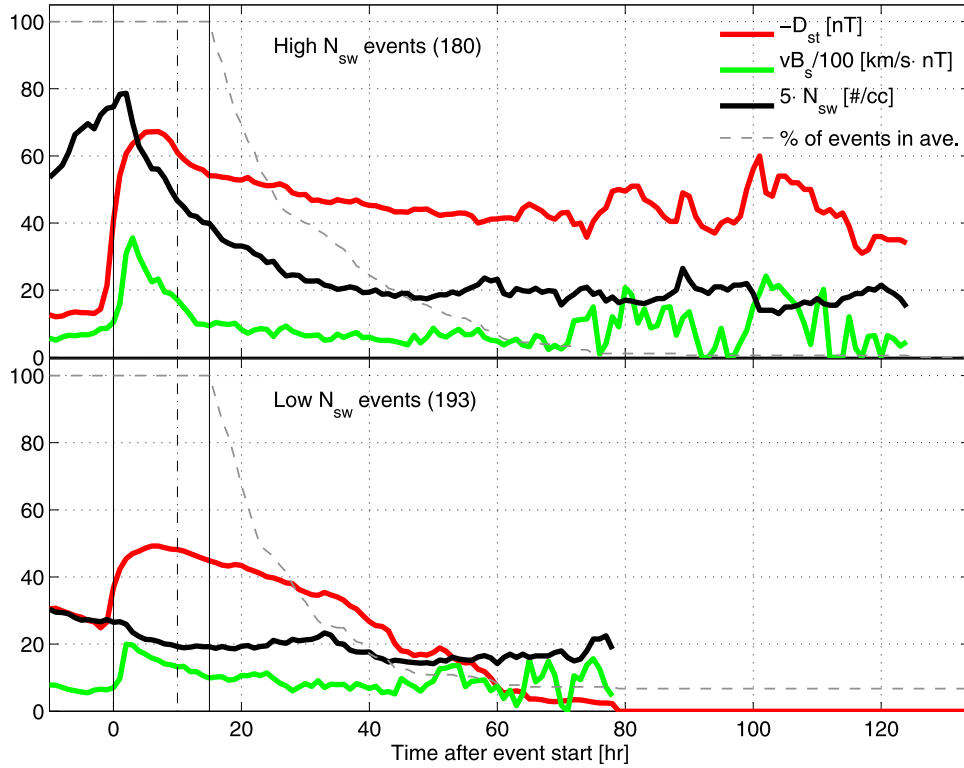
Figure 8. Epoch averages of events shown in Figure 7. The first dark vertical line indicates epoch zero, defined as when D_{st} for each event went below -30 nT. The second dark vertical is at 15 h, which was the minimum amount of time for an event to be included in the analysis. The dash-dot vertical line is at 10 h; events were sorted according to their average value of N_{sw} from epoch time zero through 10 h.

tions were identical, the integrated value of D_{st} of an IRF model derived using high N_{sw} data is predicted to be nearly twice that for IRFs derived using low N_{sw} data.

[41] The uncertainty in the slopes of each line in Figure 9a was found to be approximately 15% from the variation found

in the best-fit slope when its computation was repeated 10 times. The variation in the slopes arises because the IRF associated with each data point is an average of 50 IRFs, each of which were generated by randomly selecting subsets of all available data, as described in section 2.1.
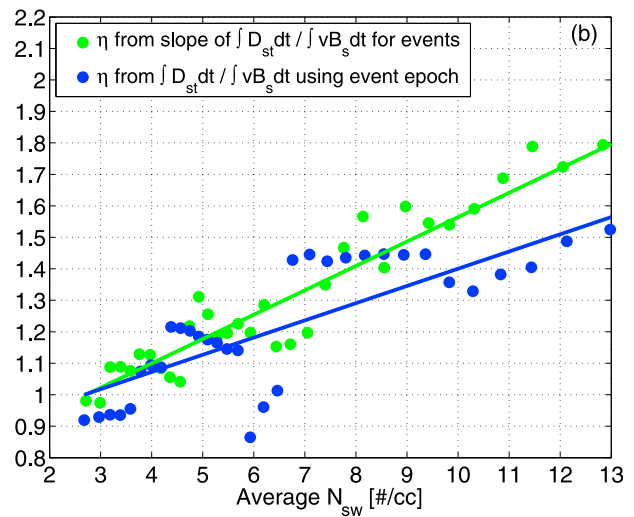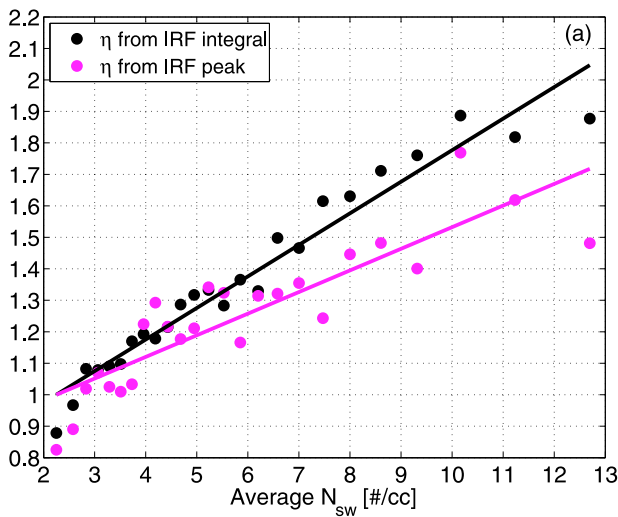
Figure 9. Computed values and best-fit line for four definitions of geoefficiency, η, as a function of N_{sw}. (a) Here η is represented by the magnitude of the peak of the impulse response function (magenta dots) or the value of the integrated impulse response function (black dots). (b) Here η is the slope of the lines in a plot similar to Figure 7 except using only 80 events to compute the slope (green dots) or the ratio the epoch averages of $-D_{st}$ and vB_s for these events computed using the approach described in the text (blue dots).

[42] The analysis of section 2.2 was repeated by sorting the 416 intervals by the cumulative value of N_{sw} from time zero to 10 h. A total of 35 windows each containing 80 events were used to generate the green points in Figure 9b. Each point is the average of 80 event integral ratios, $\int D_{st} dt / \int vB_s dt$, where the integration is taken over the full time of each event, which starts when $-D_{st}$ crosses from above to below -30 nT and ends when $-D_{st}$ crosses above -30 nT.

[43] Another approach is to compute epoch averages of D_{st} and vB_s using the 80 events and then define the ratio of the areas under the epoch curves from epoch time of zero to 15 h as a measure of geoefficiency. Calculation of the integrals of D_{st} and vB_s were done after subtracting off their epoch zero value.

[44] For arbitrary time series, this ratio of epoch average integrals approach (given by blue dots in Figure 9b) will not necessarily give the same result as the average of integral ratios approach (given by green dots in Figure 9b). The ratio of epoch average integrals approach is the one that has traditionally been used, often implicitly, in the literature when geomagnetic efficiency is discussed. We believe that the average of integral ratios approach makes more sense physically and is more robust from a statistical perspective but have provided the results from both methods here for comparison.

[45] The uncertainty in the slopes of each line in Figure 9b was estimated to also be approximately 20%, which was determined by the variation found in the best-fit slope when its computation was repeated using 60 and 100 events per epoch average instead of 80 events and by shifting the time series of the three parameters ±1 hour relative to each other before any computations were performed.

[46] All four approaches yield a general increase in a measure of efficiency with respect to N_{sw}. Although the slopes shown in Figure 9 have error bars on the order of only ±15–20%, observing this dependence will be difficult when only a few storms or short time intervals are studied. The slopes in Figure 9b are the result of averages over many storms and the storm-to-storm variability is large (which is evidenced by the scatter shown in Figure 7). Our conclusion is that Figure 9 shows (1) the response efficiency of the magnetosphere is dependent on the solar wind density; (2) the efficiency changes by approximately a factor of 1.5–2.0 for N_{sw} from 3.0 to 13.0/cm^3; and (3) identifying this efficiency dependence in a statistically meaningful way requires the analysis of over ~100 storms because the storm-to-storm variability is so large.

4. Discussion

[47] We have established that there is a difference in geoefficiency in the response of D_{st} to the solar wind electric field for different N_{sw} levels using two statistical approaches. In this section we review previous results and discuss them in the context of our findings.

[48] *Wu and Lundstedt* [1997] used a neural network filter with inputs of many combinations of solar wind variables. They found a decrease in the mean-squared error by 1.3 nT when the inputs were [N_{sw}, v, B_s] versus [v, B_s]. One possible form of or solution to this filter is an IRF separated according to density, as used in section 2.1, so it is expected that our

model should also show an improvement when density is accounted for. To compare results, we have computed two IRFs, one that is independent of N_{sw} (all data used to generate the IRF) and one that uses either the high or low impulse response filters shown in Figure 3a for a predictor, depending on whether N_{sw} is low or high. Consistent with *Wu and Lundstedt* [1997], we find that the N_{sw}–dependent model yields a mean-squared error decrease, in our case the decrease was 0.6 nT. Our interpretation of the *Wu and Lundstedt* [1997] result is that part of the improvement observed was a result of the neural network capturing a N_{sw}-dependence similar to that found in this work.

[49] *O'Brien and McPherron* [2000] showed that the *Smith et al.* [1999] finding of a N_{sw} influence on the ring current for mild storms (minimum D_{st} in the range of -50 and -200 nT) did not hold when a larger data set was used. One reason for the difference between the *O'Brien and McPherron* [2000] result and that of *Wu and Lundstedt* [1997] and this work may lie in the fact that *Smith et al.* [1999] and *O'Brien and McPherron* [2000] used a bilinear correlation model whereas *Wu and Lundstedt* [1997] used a neural network filter and we have used an impulse response filter, both of which are more general than a bilinear correlation model.

[50] *Wang et al.* [2003] computed a pressure-dependent decay time of D_{st} of a model based on equation (1). Given the finding that the impulse response function primarily depends on the solar wind density and not velocity, this result may be due to the density effect on response shown in Figure 3a. In addition, we note that the decay profile in the low-density and high-density cases in Figure 3a is not simple. The decay profiles are similar only for the first 3 h. The shape of these response functions may explain why modifications to the decay constant typically yield improved predictions of D_{st} [*Wang et al.*, 2003; *Xie et al.*, 2008]. The base model of equation (1) has exponential decay, but the data-derived impulse response functions are not exponential, which was shown in Figure 3c. The impulse response curve for equation (1) falls faster than that shown in Figure 3a. One way of slowing down or modifying the exponential decay of equation (1) is to have the time constant parameter increase during high activity by making it dependent on a variable that is correlated with high activity, such as solar wind pressure.

[51] *Lavraud et al.* [2006] considered both CME- and CIR-driven storms according to whether the IMF was southward prior to the storm. They found that the epoch average of storms with prior northward or horizontal IMF tended to be underpredicted by a modified version of equation (1). They noted that the observed differences were on the order of the error bars. This is consistent with our result that most large storms fall into the high-density category and that in order to clearly see the effect, many storms must be studied having a wide variation in N_{sw} conditions.

5. Conclusions

[52] The geoefficiency of the response of the ring current, as indicated by the proxy of D_{st}, to the solar wind electric field, vB_s, is highly dependent on the solar wind density. Two definitions of geoefficiency were considered. The first was the minimum value of a data-derived impulse response function that related D_{st} to the solar wind electric field. The

second definition was based on the ratio of the integrated value of D_{st} to vB_s during geomagnetic storm intervals. Impulse response functions derived using only data from intervals where the density was above the median have a peak and integrated magnitude that is ~1.5 times larger than those derived using only below-median data. A survey of geomagnetic storm-like intervals shows that the magnitude of their integrated value can be ~1.5 larger for a given vB_s when the solar wind density is high.

[53] If only very large storms are studied, the solar wind density effect is expected to be smaller. Geoefficiency tends to increase with average solar wind density, but the largest storms mostly fall in a density range where there is not enough variation in geoefficiency for the effect to be statistically significant unless hundreds of storms are considered.

[54] When an impulse response model is used, which incorporates the time lags inherent in the D_{st} response to solar wind variations, the solar wind electric field gives the best results or results that are equal to more complex coupling functions that have been suggested. The results of this work indicate that (1) the appropriate place for N_{sw} to appear in a model may be in the transfer function instead of the coupling function; (2) if a correlation study does not include time delays, complex coupling functions will be better predictors than simply the solar wind electric field, but their advantage diminishes when time delays are included in the model; and (3) the impulse response dependence on N_{sw} and $P_{dyn} = N_{sw}v^2$ is nearly the same, while v shows little dependence, indicating that differences in geoefficiency are best explained by a process that only involves N_{sw}.

[55] There have been several recent attempts to identify the role of the plasma sheet density, N_{ps}, on geomagnetic storms. In this work, we have only considered N_{sw}. Although N_{sw} does not have a simple and direct relationship to N_{ps}, the results shown here may have a bearing on the approach that is taken to identify a D_{st} dependence on N_{ps} if direct measurements of N_{ps} are used. In this work we have shown the importance of including a time delay in the model and the potential for a bias toward high-density behavior when only studying large storms because vB_s during storm-like events covaries with N_{sw}.

[56] An alternative explanation of the change in geoefficiency is that under the low-density solar wind conditions, ring current energy is diverted into another magnetospheric system, such as the auroral electrojects. This diversion is difficult to measure in part because it requires global measurements along with approximations of how the measurements relate to energy dissipation. Under the assumption that the amount of energy transferred to auroral Joule heating and ring current energy was constant, *Mac-Mahon and Gonzalez* [1997] estimated that during four superstorms the ring current-associated energy was one-half of the Joule heating-associated energy and this ratio was opposite of that found during active, but nonsuperstorm, periods.

References

Borovsky, J. E., and M. H. Denton (2006), Differences between CME-driven storms and CIR-driven storms, *J. Geophys. Res.*, *111*, A07S08, doi:10.1029/2005JA011447.

Borovsky, J. E., M. F. Thomsen, and R. C. Elphic (1998), The driving of the plasma sheet by the solar wind, *J. Geophys. Res.*, *103*, 17,617–17,640.

Boudouridis, A., E. Zesta, L. R. Lyons, P. C. Anderson, and D. Lummerzheim (2005), Enhanced solar wind geoeffectiveness after a sudden increase in dynamic pressure during southward IMF orientation, *J. Geophys. Res.*, *110*, A05214, doi:10.1029/2004JA010704.

Burton, R. K., R. L. McPherron, and C. T. Russell (1975), An empirical relationship between interplanetary conditions and Dst, *J. Geophys. Res.*, *80*, 4204–4214.

Jordanova, V. K., L. M. Kistler, M. F. Thomsen, and C. G. Mouikis (2003), Effects of plasma sheet variability on the fast initial ring current decay, *Geophys. Res. Lett.*, *30*(6), 1311, doi:10.1029/2002GL016576.

Kamide, Y., N. Yokoyama, W. Gonzalez, B. T. Tsurutani, I. A. Daglis, A. Brekke, and S. Masuda (1998), Two-step development of geomagnetic storms, *J. Geophys. Res.*, *103*, 6917–6922.

King, J. H., and N. E. Papitashvili (2005), Solar wind spatial scales in and comparisons of hourly Wind and ACE plasma and magnetic field data, *J. Geophys. Res.*, *110*, A02104, doi:10.1029/2004JA010649.

Lavraud, B., M. F. Thomsen, J. E. Borovsky, M. H. Denton, and T. I. Pulkkinen (2006), Magnetosphere preconditioning under northward IMF: Evidence from the study of coronal mass ejection and corotating interaction region geoeffectiveness, *J. Geophys. Res.*, *111*, A09208, doi:10.1029/2005JA011566.

Liemohn, M. W., J. U. Kozyra, M. F. Thomsen, J. L. Roeder, G. Lu, J. E. Borovsky, and T. E. Cayton (2001), Dominant role of the asymmetric ring current in producing the stormtime *Dst**, *J. Geophys. Res.*, *106*, 10,883–10,904.

Lopez, R. E., M. Wiltberger, S. Hernandez, and J. G. Lyon (2004), Solar wind density control of energy transfer to the magnetosphere, *Geophys. Res. Lett.*, *31*, L08804, doi:10.1029/2003GL018780.

Mac-Mahon, R. M., and W. D. Gonzalez (1997), Energetics during the main phase of geomagnetic superstorms, *J. Geophys. Res.*, *102*, 14,199–14,208.

Newell, P. T., T. Sotirelis, K. Liou, and F. J. Rich (2007), A nearly universal solar wind-magnetosphere coupling function inferred from 10 magnetospheric state variables, *J. Geophys. Res.*, *112*, A01206, doi:10.1029/2006JA012015.

O'Brien, T. P., and R. L. McPherron (2000), Evidence against an independent solar wind density driver of the terrestrial ring current, *Geophys. Res. Lett.*, *27*, 3797–3800.

O'Brien, T. P., and R. L. McPherron (2002), Seasonal and diurnal variation of Dst dynamics, *J. Geophys. Res.*, *107*(A11), 1341, doi:10.1029/2002JA009435.

Perreault, P., and S.-I. Akasofu (1978), A study of geomagnetic storms, *Geophys. J.*, *54*, 547–573.

Richardson, I. G., H. V. Cane, and E. W. Cliver (2002), Sources of geomagnetic activity during nearly three solar cycles (1972–2000), *J. Geophys. Res.*, *107*(A8), 1187, doi:10.1029/2001JA000504.

Shi, Y., E. Zesta, L. R. Lyons, A. Boudouridis, K. Yumoto, and K. Kitamura (2005), Effect of solar wind pressure enhancements on storm time ring current asymmetry, *J. Geophys. Res.*, *110*, A10205, doi:10.1029/2005JA011019.

Shue, J. H., and Y. Kamide (2001), Effects of solar wind density on auroral electrojets, *Geophys. Res. Lett.*, *28*, 2181–2184.

Shue, J.-H., Y. Kamide, and P. T. Newell (2005), A systematic study of effects of solar wind density on auroral electrojets, *Geophys. Res. Lett.*, *32*, L14112, doi:10.1029/2005GL023197.

Siscoe, G. L., G. M. Erickson, B. U. Ö. Sonnerup, N. C. Maynard, J. A. Schoendorf, K. D. Siebert, D. R. Weimer, W. W. White, and G. R. Wilson (2002), Hill model of transpolar potential saturation: Comparisons with MHD simulations, *J. Geophys. Res.*, *107*(A6), 1075, doi:10.1029/2001JA000109.

Smith, J. P., M. F. Thomsen, J. E. Borovsky, and M. Collier (1999), Solar wind density as a driver for the ring current in mild storms, *Geophys. Res. Lett.*, *26*, 1797–1800.

Thomsen, M. F., J. E. Borovsky, R. M. Skoug, and C. W. Smith (2003), Delivery of cold, dense plasma sheet material into the near-Earth region, *J. Geophys. Res.*, *108*(A4), 1151, doi:10.1029/2002JA009544.

Vassiliadis, D., A. J. Klimas, and D. N. Baker (1999), Models of d-st geomagnetic activity and of its coupling to solar wind parameters, *Phys. Chem. Earth C*, *24*, 107–112.

Wang, C. B., J. K. Chao, and C.-H. Lin (2003), Influence of the solar wind dynamic pressure on the decay and injection of the ring current, *J. Geophys. Res.*, *108*(A9), 1341, doi:10.1029/2003JA009851.

Weigel, R. S. (2007), Solar wind time history contribution to the day-of-year variation in geomagnetic activity, *J. Geophys. Res.*, *112*, A10207, doi:10.1029/2007JA012324.

Wu, J.-G., and H. Lundstedt (1997), Geomagnetic storm predictions from solar wind data with the use of dynamic neural networks, *J. Geophys. Res.*, *102*, 14,255–14,268.

Xie, H., N. Gopalswamy, O. C. St. Cyr, and S. Yashiro (2008), Effects of solar wind dynamic pressure and preconditioning on large geomagnetic storms, *Geophys. Res. Lett.*, *35*, L06S08, doi:10.1029/2007GL032298.

R. S. Weigel, Department of Computational and Data Sciences, George Mason University, 4400 University Drive, Fairfax, VA 22030, USA. (rweigel@gmu.edu)